SUPPLEMENTAL MATERIAL

Fault gouge melting at shallow depth during the 2008 Mw 7.9 Wenchuan earthquake

H. Wang[1,2,3], H.B. Li[1,2,3*], G. Di Toro[4,5], L.-W. Kuo[6], E. Spagnuolo[5], S. Aretusini[5], J.L. Si[1,2,3], S.-R. Song[7]

[1]*MNR Key Laboratory of Deep-Earth Dynamics, Institute of Geology, Chinese Academy of Geological Sciences, Beijing 100037, China*
[2]*Southern Marine Science and Engineering Guangdong Laboratory (Guangzhou), Guangzhou 511458, China*
[3]*Jiangsu Donghai Continental Deep Hole Crustal Activity National Observation and Research Station, Jiangsu 222300, China*
[4]*Dipartimento di Geoscienze, Università di Padova, Padova 35131, Italy*
[5]*Istituto Nazionale di Geofisica e Vulcanologia, Rome 00143, Italy*
[6]*Department of Earth Sciences, National Central University, Taoyuan 32001, Taiwan*
[7]*Department of Geosciences, National Taiwan University, Taipei 10617, Taiwan*

*Correspondence to: lihaibing06@163.com

Coseismic Surface Rupture Zones of the 2008 Wenchuan earthquake

Two coseismic surface rupture zones were produced at the southern segment of the Yingxiu-Beichuan fault, one was along the Yingxiu fault, and the other was along the Shenxigou fault (Fig. S1). These two branches merged into one rupture zone at the Bajiaomiao village, where two sets of coseismic striations could be seen in the fault scarp (Pan et al., 2014).
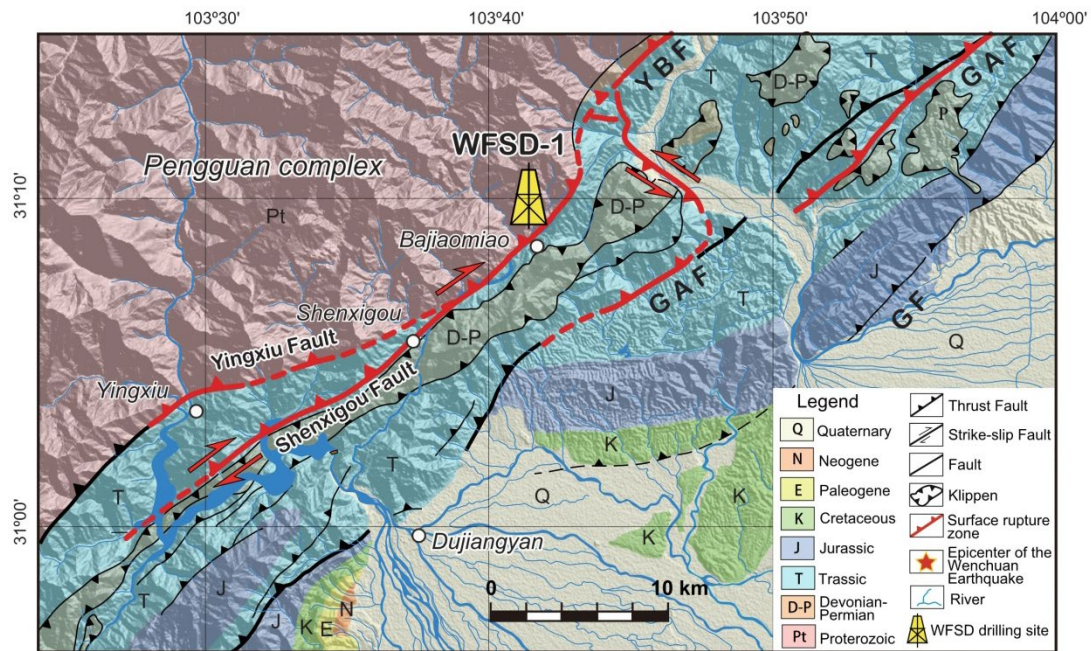

Figure S1. Coseismic surface rupture zones of the 2008 Wenchuan earthquake at the southern segment of the Yingxiu-Beichuan fault. The surface rupture zone along the Yingxiu fault is nearly pure thrust without a horizontal component, and the Shenxigou fault branch is featured by thrusting with right-lateral strike-slip movement. YBF: Yingxiu-Beichuan fault, GAF: Guanxian-Anxian fault, GF: Guankou fault.

Sample Collection and Preparation

The sample we studied was collected from the drilling core numbered B330R110-2 (732.4-733.33 m-depth), which was recovered on 9th May 2009, nearly one year after the Wenchuan earthquake. The core was wrapped in preservative film after being cleaned by water and dried naturally, and then stored at room temperature in the core repository.

The drilling core was split into two halves, the one with lines marked the top and bottom was documented, and the other half was used to study. The studied sample was impregnated with epoxy resin, and cut across the diameter of the sample and

perpendicular to the slip surface, to produce 30-μm-thick petrographic thin sections. Fourteen thin sections were made from this drill core (Fig. S2). After observation with an optical microscope, the thin section was coated with carbon to increase the electrical conductivity for scanning electron microscopy analysis. The TEM sample was prepared by focus ion beam (FIB), coated with platinum.
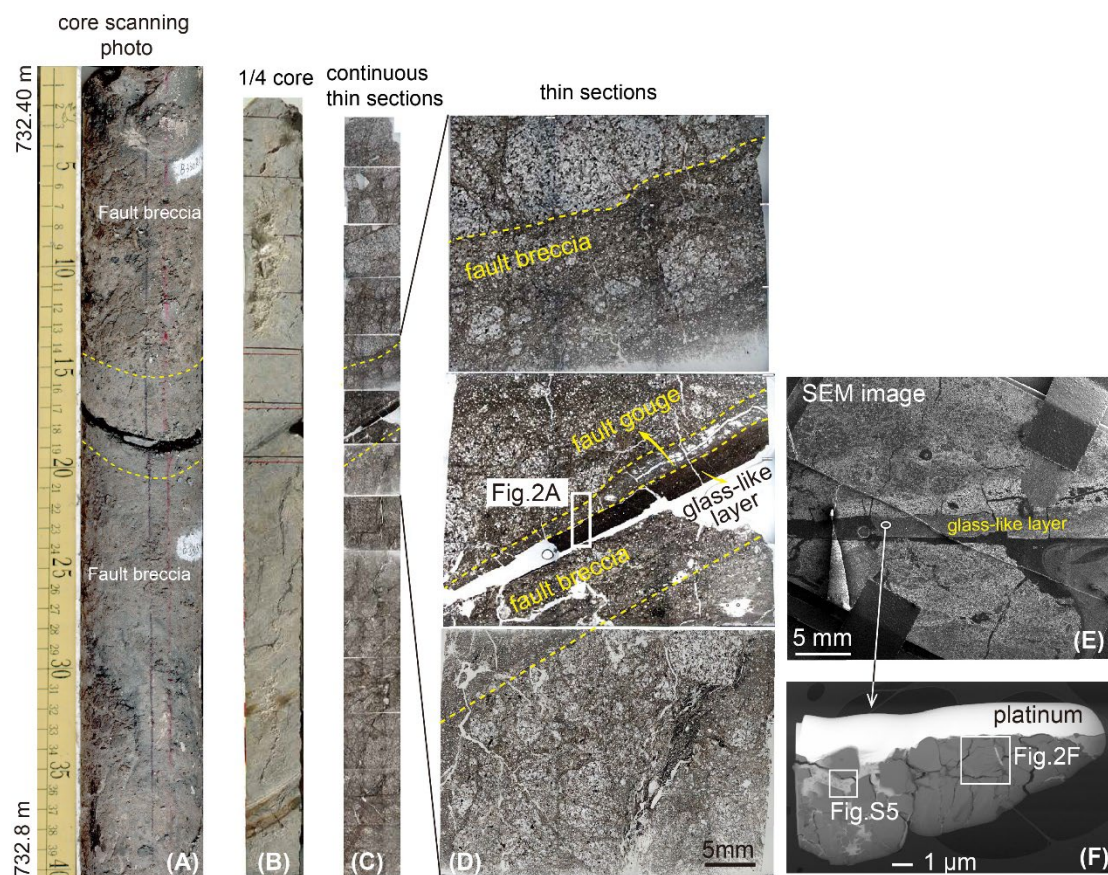

Figure S2 Sample preparation. A: The drilling core scanning photo with markers. B:1/4 core was used to make thin sections. C: the corresponding thin sections made from B. D: fault rocks near the PSZ, the white box indicates the location of Fig. 2A. E: SEM image shows the location where the TEM sample was taken. F: The TEM sample was prepared by FIB. The boxes show where Fig. 2F and Fig. S5 are.

Mineral Composition of the Fault Rocks Collected from the WFSD-1

X-ray diffraction (XRD) analyses were conducted on nine samples retrieved at 704-733 m depth in the WFSD-1 borehole. The XRD diffraction patterns and the semi-quantitative analysis are reported in Fig. S3 and Table S1, respectively. These fault rocks have a similar mineralogical composition with limited variations in mineral abundance. In all the samples quartz is the main phase, with minor plagioclase and K-feldspar. Phyllosilicates are white mica (phengite or muscovite)

and chlorite. Other minor phases include calcite and dolomite whose abundance is variable in the samples. In particular, dolomite is represented by two phases with slightly different compositions (possible zonation), and one of these two is possibly dolomite with excess Ca or Fe (Fe-rich dolomite or ankerite). Also, traces of pyrite are present. In the diffraction spectrum, the higher background at $2\theta < 10°$ can indicate the presence of poorly crystalline clays (interstratified smectite-illite with a very small crystallite size). The background between $15 < 2\theta < 25°$ increases progressively from DH-11 to DH-21. This increase can be related to the increase of the amorphous component approaching the principal slip zone located at 732.6 m.

Table S1. Mineralogical composition (wt.%, semi-quantitative analysis) of the fault rocks from WFSD-1.

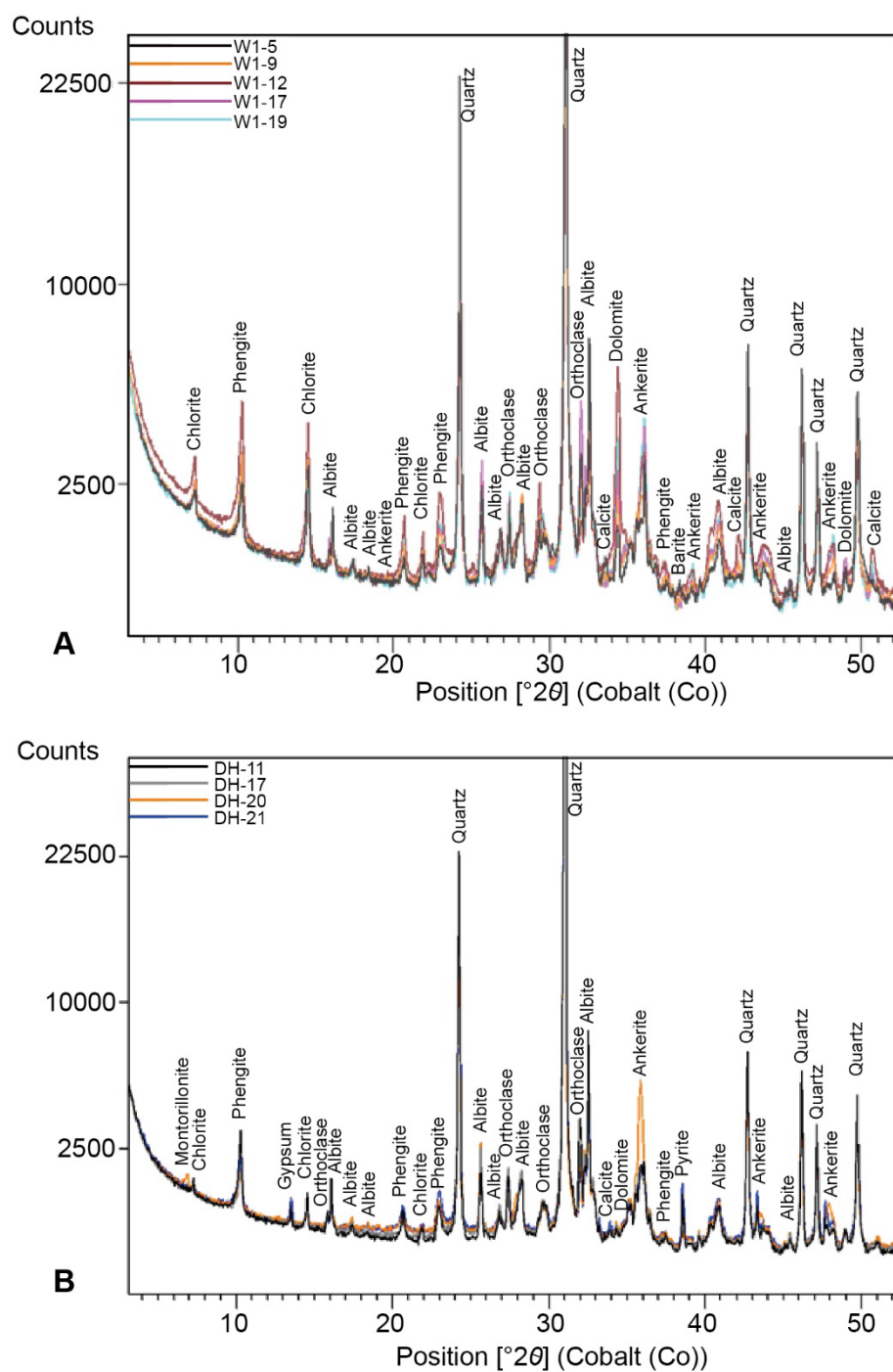| Sample	WI-5	WI-9	WI-12	WI-17	WI-19	DH-11	DH-17	DH-20	DH-21
Depth	704.06	706.73	708.2	719.43	728.3	732.1	732.46	732.54	732.58
Lithology	Fault breccia	Fault breccia	Fault breccia	Fault breccia	Fault breccia	Fault breccia	Fault breccia	Fine-grain fault breccia	Fault gouge
Quartz	75	75	63	71	74	71	74	71	74
Albite	7	8	5	9	8	10	12	11	8
Orthoclase	4	4	4	4	2	6	5	5	3
Phengite	3	4	11	5	3	3	2	2	2
Dolomite	4	2	3	3	3	2	1	2	1
Ankerite	1	2	3	2	2	2	2	6	3
Calcite	1	2	6	3	3	1	1	1	1
Chlorite	3	3	6	3	3	2	2	2	2
Pyrite						3	2		4
Gypsum						1			2
Barite	1								
Montorillonite								<1	

Figure S3. X-ray diffraction patterns of the fault rocks from the WFSD-1 drilling cores. A: Diffraction patterns for samples of W1 series from 704.06 to 728.30 m-depth. B: Diffraction patterns for samples of DH series from 732.10 to 732.58 m-depths.
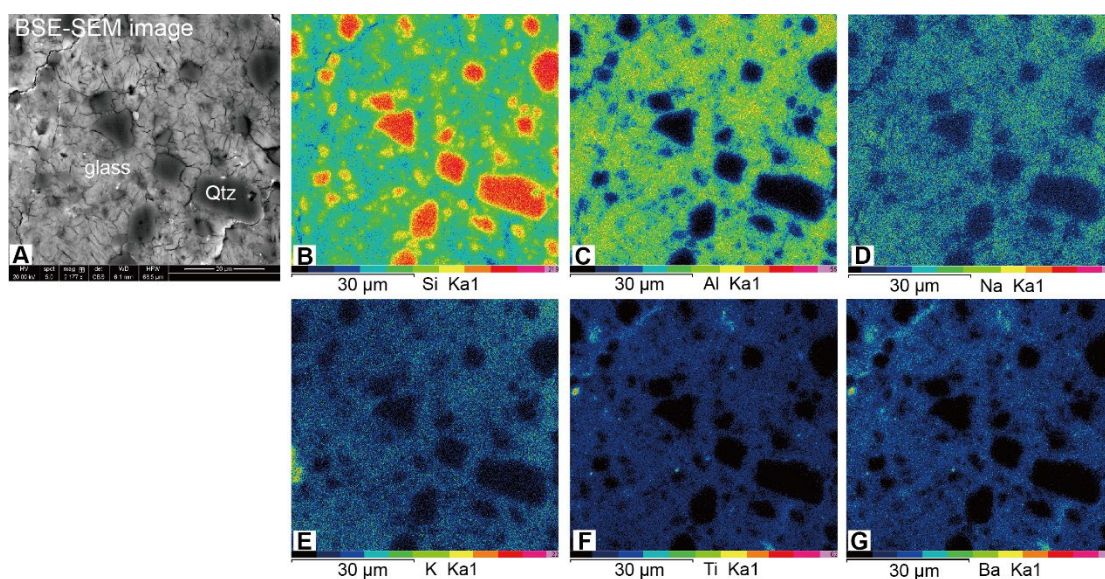
Figure S4. Single element maps of the glass-like layer at 732.6 m depth in the WFSD-1 drilling cores (SEM-EDX analysis on the thin section). A: BSE-SEM image with quartz clasts bounded by a whitish glass-like matrix cut by microcracks. B-G: Single element maps of Si, Al, Na, K, Ti, and Ba.
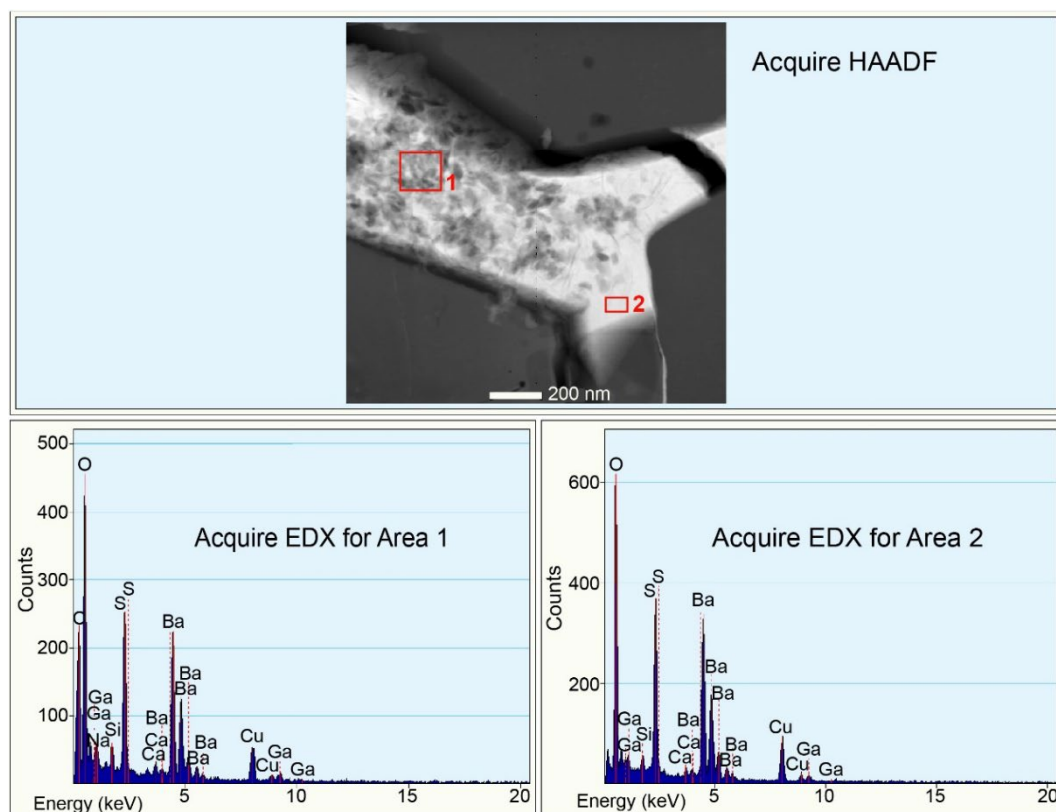

Figure S5 TEM-EDX analyses of the micro veins cutting the glass-like matrix.

Rotary Shear Friction Experiments

Rotary shear friction experiments were performed on the fault breccias retrieved from the WFSD-1 drilling cores with the aim of reproducing the estimated coseismic slip conditions at the borehole depth of 732.6 m (the depth where the glass-like layer was recognized in the borehole). The fault breccias, which have a similar mineralogical composition to the fault rocks from 732.6 m (Table S1 and Fig. S3), were gently crushed and sieved to < 250 μm in size and poured into a ring-shaped sample holder (Fig. S6A) designed for non-cohesive fault gouge materials (Smith et al., 2013) using steel ("steel+steel", Table S2) or tungsten carbide forcing blocks ("WC+steel", Table S2). Alternatively, granite forcing blocks and Teflon confining rings (Mizoguchi et al., 2007) were used ("rock+Teflon", Table S2). Fault gouges were sheared at an imposed slip velocity of 1 m/s for up to 5 m of slip, under room humidity or fluid-rich conditions, the latter obtained by adding 20 wt.% distilled water (Table S2). As a water content of 20 wt.% was required to dampen the gouge and more water than this content would result in experimental failure because the gouges were not fully confined.

The applied normal stress was 20 MPa to approach the stress normal to the fault. In fact, Anelastic Strain Recovery analysis performed on the WFSD-1 cores recovered at 682 m and 760 m depths (i.e., above and below the fault gouge with the glass-like layer) in the Xujiahe Fm., yielded post-seismic maximum horizontal stress of 21.6 and 25.0 MPa, minimum horizontal stresses of 18.5 and 21.1 MPa and vertical stresses of 17.1 and 19.1 MPa (Cui et al., 2014). The extrapolation of these stress magnitudes to 732 m depth would correspond to maximum horizontal, minimum horizontal and vertical stresses of 24.0, 20.4, and 18.2 MPa, respectively. The resulting differential stress (maximum horizontal minus vertical stresses) at 732 m depth would be 5.8 MPa. The orientation and magnitude of the three stresses are consistent with thrust kinematics with maximum compression oriented N310 (ca. orthogonal to fault strike). Given the dip angle of the thrust of 65° at 732.6 m depth, the stress normal to the fault is 23 MPa (http://www.geo.cornell.edu/geology/faculty/RWA/programs/mohrplotter.html). However, this estimate is based on the stress tensor analysis made in the borehole *after* the Mw 7.9 earthquake. Feng et al (2016) estimated a static stress change of ~2 MPa at 1200 m depth in the WFSD-1 associated with the Wenchuan 2008 Mw 7.9 earthquake. So the magnitude of the stress normal to the fault *before* the earthquake in this area was probably slightly larger than 23 MPa. However, Cui et al. (2014) suggested that the small differential stress (e.g., 5.8 MPa at 732.6 m depth) and the rotation of the principal stresses towards the extensional regime in the top 424 m of the rock volume drilled by WFSD-1, are consistent with almost total coseismic stress

drop. Given that the variation of the vertical stress is small in a thrust earthquake, a large stress drop would imply a large maximum horizontal stress and, consequently, a stress normal to the fault of 40-50 MPa. Last but not the least, the fault is severely misoriented for fault reactivation (Zhang, 2013). Given also the lack of pore pressure measurements, the determination of the *in-situ* effective stress normal to the fault at the time of the earthquake remains challenging. Deformed samples (Fig. S6B) were collected for microstructural investigations (experiments S1541 and S1547).

Table S2 List of experiments (all experiments performed at 20 MPa normal stress).

Exp.No.	Sample	Id	Mass	Humidity	Velocity	Slip distance	Sample holder
			g		m/s	m	
S1541	grey breccia	W1-9	5.0	room humidity	1	4.5	WC+steel
S1542	dark grey breccia	W12	5.0	room humidity	1	5.0	WC+steel
S1543^	grey breccia	W1-9	8.0	room humidity	1	5.0	WC+steel
S1545^	grey breccia	W1-9	5.65	room humidity	1	4.0	rock+Teflon
S1547^	grey breccia	W1-10	8.0	20wt.% water added	1	3.0	steel+steel
S1891^	grey breccia	DH1-8	8.0	20wt.% water added	1	2.75	steel+steel

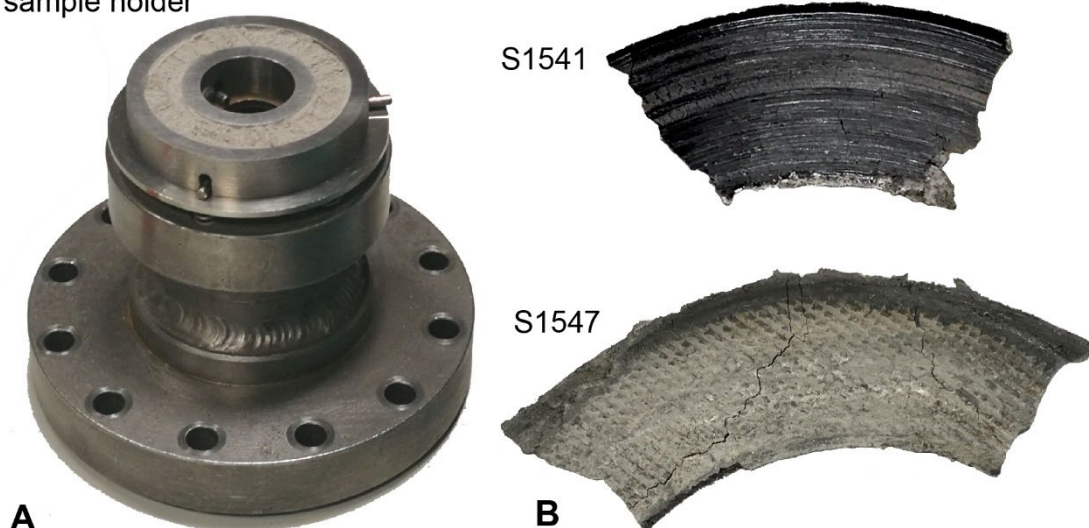^ experiments with preshear at 10^{-5} m/s for 0.01 m of slip

Figure S6 A: Gouge sample holder (here is shown the WC (tungsten-carbide)-steel-made described in Smith et al. (2013). B: experimental deformed products of S1541 (under room humidity condition) and S1547 (under water-dampened condition)

The measured apparent friction coefficient is presented in Fig. S7. Under room humidity conditions, the friction coefficient evolves from a value of ca. 0.6-0.7 at the onset of sliding down to ~0.2 (S1545, rock+rock Teflon-confined gouge holder) or ~0.4-0.5 to ~0.3 (S1541 and S1543, WC+steel gouge holder) at 2-2.75 m of slip (Fig. S7A). The lower friction coefficient measured in S1545 can be explained by the lower thermal conductivity of the gouge holder with respect to the WC+steel gouge holder used in S1541 and S1543. In fact, the lower thermal conductivity of the rock+rock Teflon-confined gouge holder allows the achievement of higher temperatures in the sheared gouge layer and lower frictional resistance compared to the lower temperatures achieved with high thermal conductivity gouge holders (Yao et al., 2016). Experiment S1542 is performed on the dark grey breccia with the WC+steel gouge holder. The friction coefficient drops from a peak value of 0.6 to a dynamic friction value of ~0.3 (Fig. S7B). Instead, under water-dampened conditions, the friction coefficient evolves from a value of ca. 0.6 at the onset of sliding, down to ~0.4 after 0.1 m of slip, and eventually to 0.3 after 1.5 m of slip (S1891, steel+steel gouge holder, Fig. S7C). The anomalies of the S1547 (steel+steel gouge holder) were due to sample extrusion during shearing.
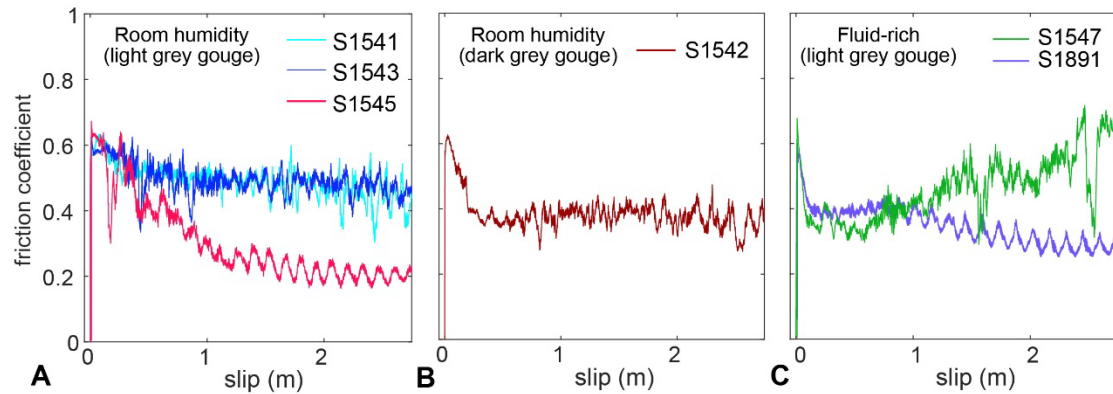

Figure S7. Experimental results from rotary shear experiments. The target slip rate in all the experiments was 1 m/s and the applied normal stress was 20 MPa. A: Room humidity conditions experiments of light grey gouge (S1541, S1543, S1545). B: Room humidity conditions experiment of dark grey gouge (S1542). C: Fluid-rich conditions experiments (S1547, S1891). All the experiments were performed with metal-built gouge holders, with the exception of experiment S1545 where the gouge was confined by two rock cylinders and by an external Teflon ring (Mizoguchi et al., 2007). The latter gouge holder has a lower thermal conductivity.

Modeling of the Alteration of the Natural Pseudotachylytes

Material

The glass alteration rate was simulated using the pseudotachylyte (SiO_2 60 wt.%) which shares a similar composition as the glassy matrix of the pseudotachylyte in the 732.6 m. The composition of the glassy matrix of the natural pseudotachylyte is reported in table S3 (the analyzed spots are shown in the SEM image of Figure. S8).
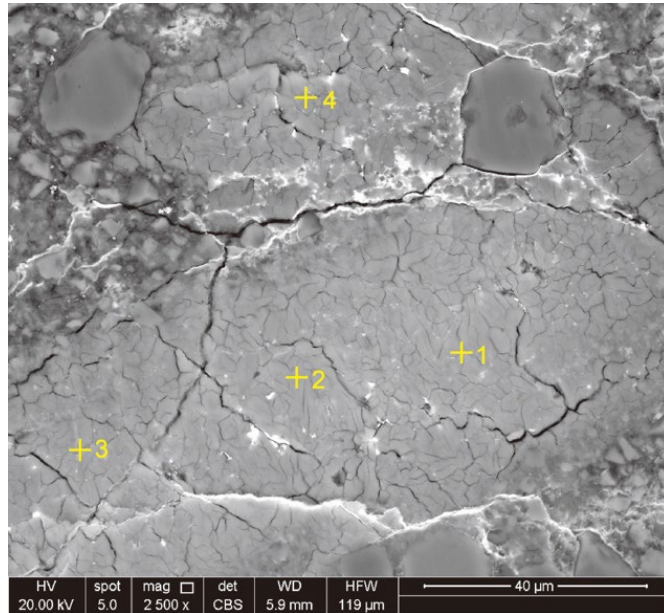

Figure S8 SEM image of the glassy matrix of the pseudotachylyte, showing the EDX analyzed spots.

Table S3. Elemental composition (wt.%) of the glassy matrix (see spots in Figure S8).

	Na_2O	Al_2O_3	SiO_2	SO_3	K_2O	BaO	MgO	Fe_2O_3
Spot 1	3.02	19.10	58.73	1.12	1.60	16.43	/	/
Spot 2	2.81	18.88	58.93	0.85	1.62	16.92	/	/
Spot 3	3.38	18.85	58.96	2.37	2.13	13.21	0.35	0.74
Spot 4	3.88	20.41	63.07	/	2.29	10.35	/	/

The SiO_2 weight percentage in the natural pseudotachylyte matrix is 58-63%. As a consequence, to model the alteration of the pseudotachylyte glass we used material containing 60 wt.% SiO_2 with SiO_2 atomic mass of 60.085, and with a density of glass of 2.65 g/cm^3.

Method

Wolff et al. (2004) investigated with dedicated experiments the dissolution rates of natural glasses in water solutions as a function of the glass composition (from basaltic to rhyolitic) at pH of 4 and 10.6, and at temperatures ranging from 25 to 74°C. Because the conditions of some of these experiments are close to the conditions in the WFSD-1 borehole at which the natural pseudotachylyte was retrieved (pH ~ 9.2 to 10.3; temperature ~ 27.5°C), we used the experimentally-constrained dissolution rates of Wolff et al. (2004) in our model.

We developed a model to estimate how fast the pseudotachylyte may alter through time at the borehole ambient conditions. In particular, the rate of alteration and dissolution of a pseudotachylyte vein depends on the composition of both the glass and the fluid, the thickness of the pseudotachylyte, the permeability of the glass, the flow rate, the surface area of contact between the glass and fluid (Morin et al., 2015). The parameters used in Wolff et al., (2004) are adopted in our modeling as reported below:

(1) Equations used:
For pH 4 solutions:

$$\log r_{+,geo} \left(\frac{mol}{m^2 s} \right) = -0.03 \cdot [SiO_2(wt.\%)] - 7.58$$

For pH 10.6 ± 0.2:

$$\log r_{+,geo} \left(\frac{mol}{m^2 s} \right) = -0.02 \cdot [SiO_2(wt.\%)] - 7.02$$

(2) Alteration temperature range:
We set up the temperature of 25°C because the modeling was experimentally

developed at that temperature (Wolff et al., 2004).

(3) Water activity:

All aqueous activities in the present study were generated using the PHREEQC 2.6

computer code (Parkhurst and Appelo, 1999). The $a_{H+}^3/a_{Al^{3+}}$ activity ratio was

assumed to keep approximately constant in all experiments. We use $\log a_{H+}^3/a_{Al^{3+}}$

for the 25°C experiments was fixed at -6.4 ± 0.6.

(4) Salinity of the fluid:

All experiments were performed at pH 4 or 10.6 and ionic strength of 10 mM. Acid
inlet solutions comprised Millipore™ water and Merck analytical grade NH_4Cl and
HCl; alkaline solutions comprised Millipore ™ water and Merck analytical grade
NH_4Cl and NH_3.

(5) Geometric surface area:

The specific surface area A_{geo} is estimated as (Brantley et al., 1999; Gautier et al.,
2001):

$$A_{geo} = \frac{6}{\rho \cdot d_{eff}}$$

where ρ is the glass density and d_{eff} is the effective particle diameter. The number 6 is
based on the assumption that grains have a regular and smooth spherical shape.
Assuming a homogeneous particle distribution, d_{eff} can be obtained from (Tester et al.,
1994):

$$d_{eff} = \frac{d_{max} - d_{min}}{\ln\left(\frac{d_{max}}{d_{min}}\right)}$$

where d_{max} and d_{min} refer to the maximum and minimum particle size of the size
fraction used in the experiments.

(6) Thermodynamic conditions:

We assume far-from-equilibrium conditions or that water is undersaturated due
to continuous flow across the altering glass.

The obtained alteration rate will be over-estimated because the geometric surface
area of our glass (compacted layer shape with micro-fissures) is less than the one used
in Wolff et al. (2004) which were regular and smooth spherical shapes. In addition,
uncertainty exists in this modeling because we cannot constrain the rate of fluid flow
at the depth and the permeability of the gouge. We can assume that we are far from
equilibrium always in a fluid-percolated fault, as suggested by the abundance of barite

veins.

Results

Figure S9 shows the time scale for dissolution of pseudotachylytes (SiO_2 60 wt.%) with different thicknesses. Fluid fluxes and permeability may be low in fault cores (Wu et al., 2020), and in the absence of fluid flow, the glass dissolution would be limited by diffusion which would slow down the rate of alteration. Therefore, the timescales presented here are minimum estimates, as they assume the continuous fluid flow of fresh seawater across the pseudotachylyte surface area. This model shows that, under the condition of Ph=10, the 2 mm-thick pseudotachylyte should remain intact within one year and will be dissolved 33% (~700 μm) within 100 years.
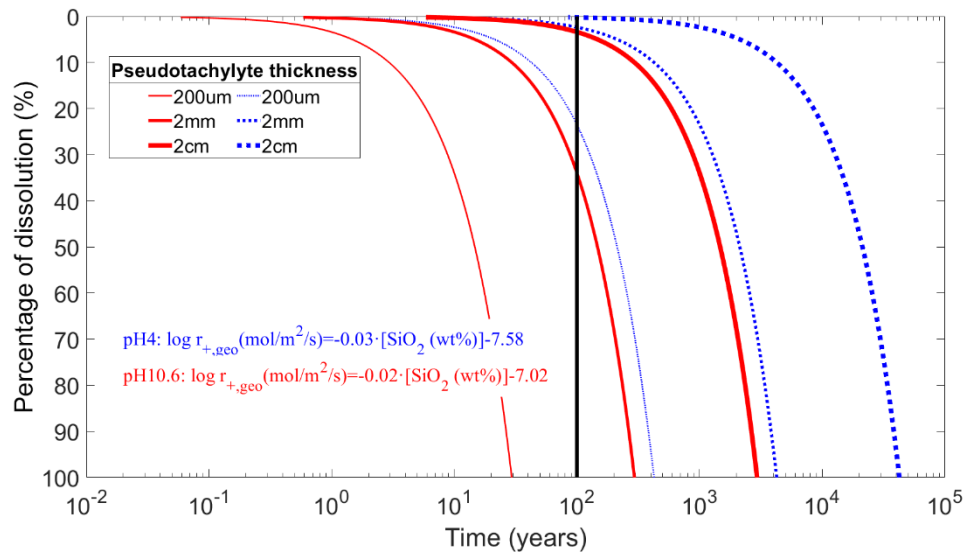

Figure S9 Dissolved percentage of pseudotachylyte with time. Pseudotachylytes in alkaline solutions have dissolution rates at least one order of magnitude higher than in acid solutions. The black line represents the time of 100 years.

References

Brantley, S.L., White, A.F., and Hodson, M.E., 1999, Surface Area of Primary Silicate Minerals. In: Jamtveit, B., Meakin, P. (eds) Growth, Dissolution and Pattern Formation in Geosystems. *Springer, Dordrecht*, p. 291–326, https://doi.org/10.1007/978-94-015-9179-9_14.

Cui, J.W., Lin, W.R., Wang, L.J., Gao, L., Wang, W., Sun, D.S., Li, Z.F., Zhou, C.J., Qian, H.S., Peng, H., Xia, K.M., and Li, K., 2014, Determination of three-dimensional in situ stresses by anelastic strain recovery in Wenchuan Earthquake Fault Scientific Drilling Project Hole-1 (WFSD-1): Tectonophysics, v. 619–620,

p. 123–132, https://doi.org/10.1016/j.tecto.2013.09.013.

Feng, C.J., Yang, Y.H., Ma, X.D., Qi, B.S., Zhang, P., Meng, J., Tan, C.X., and Chen, Q.C., 2020, Local stress perturbations associated with the 2008 Wenchuan M 8.0 earthquake near the Longmenshan fault zone in the eastern margin of the Tibetan Plateau: Journal of Asian Earth Sciences, v. 200, 104429, https://doi.org/10.1016/j.jseaes.2020.104429.

Mizoguchi, K., Hirose, T., Shimamoto, T., and Fukuyama, E., 2007, Reconstruction of seismic faulting by high-velocity friction experiments: An example of the 1995 Kobe earthquake: Geophysical Research Letters, v. 34, L01308, https://doi.org/10.1029/2006GL027931.

Morin, G.P., Vigier, N., and Verney-Carron, A., 2015, Enhanced dissolution of basaltic glass in brackish waters: Impact on biogeochemical cycles: Earth. Planet. Sci. Lett., v. 417, p. 1–8, https://doi.org/10.1016/j.epsl.2015.02.005.

Pan, J.W., Li, H.B., Si, J.L., Pei, J.L., Fu, X.F., Chevalier, M.L., and Liu, D.L., 2014, Rupture process of the Wenchuan earthquake (Mw 7.9) from surface ruptures and fault striations characteristics: Tectonophysics, v. 619–620, p. 13–28, https://doi.org/10.1016/j.tecto.2013.06.028.

Parkhurst, D.L., and Appelo, C.A.J., 1999, User's guide to PHREEQC (Version 2)—A computer program for speciation, batch-reaction, one-dimensional transport, and inverse geochemical calculations. *U. S. G. S. Wat. Res. Inv. Report.* p. 99–4259, https://doi.org/10.3133/wri994259.

Smith, S.A.F., Di Toro, G., Kim, S., Nielsen, S., Billi, A., and Spiess, S., 2013, Coseismic recrystallization during shallow earthquake slip: Geology, v. 41, p. 63–66, https://doi.org/10.1130/G33588.1.

Tester, J.W., Worley, W.G., Robinson, B.A., Grigsby, C.O., and Feerer, J.L., 1994, Correlating quartz dissolution kinetics in pure water from 25 to 625°C: Geochim. Cosmochim. Acta, v. 58, p. 2407–2420, https://doi.org/10.1016/0016-7037(94)90020-5.

Wu, W-J., Kuo, L-W., Ku, C-S., Chiang, C-Y., Sheu, H-S., Aprilniadi, T.D., and Dong, J-J., 2020, Mixed-mode formation of amorphous materials in the creeping zone of the Chihshang fault, Taiwan, and implications for deformation style: J. Geophys. Res., v. 125, p. 1-19, https://doi.org/10.1029/2020JB019862.

Yao, L., Ma, S.L., Platt, J.D., Niemeijer, A.R., and Shimamoto, T., 2016, The crucial role of temperature in high-velocity weakening of faults: Experiments on gouge using host blocks with different thermal conductivities: Geology, v. 44, p. 63–66, https://doi.org/10.1130/G37310.1